JOURNAL OF PROPULSION AND POWER
Vol. 18, No. 3, May–June 2002

Combustion of Liquefying Hybrid Propellants: Part 1, General Theory

M. A. Karabeyoglu,* D. Altman,† and B. J. Cantwell‡
Stanford University, Stanford, California 94305

In this paper classical hybrid combustion theory is generalized to solid fuels that form a liquid layer on their burning surface. For several classes of liquefying fuels, the layer is hydrodynamically unstable in a gas flow environment leading to substantial droplet entrainment into the gas stream. The susceptibility of a given fuel to this shear driven instability increases with decreasing viscosity and surface tension of the melt layer. The entrainment mass transfer, which acts in addition to the conventional gasification mechanism, is not affected by the blocking phenomenon induced by blowing from the surface. For practical oxidizer flux levels encountered in hybrid rocket applications, droplet entrainment can dominate direct gasification. Such liquefying fuels can exhibit greatly increased surface regression rates compared to classical materials such as Hydroxyl Terminated Polybutadiene. One application of the theory is to solid cryogenic hybrids, which utilize frozen materials for the solid propellant. The theory successfully predicts why high regression rates are observed in tests of cryogenic solid pentane, solid methane, and solid oxygen. In addition, the theory explains the dependence of the burning rates of other tested cryogenic materials on the physical properties of the liquid layer. The theory also leads to the conclusion that certain noncryogenic materials such as paraffin and Polyethylene waxes will also exhibit high regression rates. This important result is confirmed by lab scale tests performed at Stanford University on a high melting point paraffin wax.

Nomenclature

A	=	radiation parameter, K
A_n	=	nozzle throat area, m^2
a	=	absorption coefficient, m^{-1}
B, B_g	=	blowing parameter and evaporation blowing parameter
C	=	specific heat, kJ/kg-s
C_{B1}, C_{B2}	=	blowing correction coefficients
C_H, C_{H0}	=	stanton number with and without blowing
c_d	=	discharge coefficient
c_f	=	skin-friction coefficient
c^*	=	characteristic velocity, m/s
e_0	=	entrainment coefficient
F_r	=	heat-transfer correction factor for surface roughness
G, $\bar{G}$	=	instantaneous mass flux, time-averaged mass flux, kg/m^2-s
h	=	melt layer thickness, mm
h_m, h_e	=	total heats of melting and entrainment, kJ/kg
h_v	=	total effective heat of gasification, kJ/kg
L	=	fuel grain length, m
L_m, L_v	=	latent heat of melting and vaporization, kJ/kg
M_f	=	total fuel mass, kg
$\dot{m}$	=	total mass flow rate (oxidizer + fuel), kg/s
$\dot{m}_{\text{ent}}$	=	entrainment component of mass flux from fuel surface, kg/m^2-s
$\dot{m}_f$, $\dot{m}_o$	=	fuel and oxidizer mass flow rates, kg/s
$\dot{m}_l$	=	mass flow rate of liquid flowing through melt layer per unit width, kg/m-s
P_c	=	chamber pressure, Pa
P_d	=	dynamic pressure in the port, Pa
$\dot{Q}_r$, $\dot{Q}_c$	=	radiative and convective heat transfer at the surface, kJ/m^2-s
$\dot{q}_r$	=	radiative energy flux, kJ/m^2-s
R	=	ratio of thermal to radiative thickness
R_h	=	ratio of effective heats of gasification for entrainment and vaporization
r_0, r_f	=	initial and final port radii, mm
$\dot{r}$, $\bar{\dot{r}}$	=	instantaneous and time-average regression rate, mm/s
$\dot{r}_{\text{cl}}$	=	regression rate predicted by classical theory, mm/s
T_a	=	initial fuel temperature, K
T_g	=	average gas phase temperature, K
T_m, T_v	=	melting and vaporization temperatures, K
t_b	=	burn-out time, s
u_l	=	liquid interface velocity, m/s
X_e	=	entrainment parameter, N$^{1/2}$
x	=	distance from the interface, m
z	=	axial distance along the port, m
α, β	=	dynamic pressure and thickness exponents
Δh	=	enthalpy difference between the flame and the surface, kJ
ΔT_1, ΔT_2	=	temperature differences, $T_v - T_m$ and $T_m - T_a$, K
δ	=	thermal thickness, mm
η_c	=	combustion efficiency
κ, λ	=	thermal diffusivity and conductivity, m^2/s and W/m-K
μ	=	viscosity, milliPa-s
ρ	=	density, kg/m^3
σ	=	surface tension, milliN/m
ϕ, φ	=	nondimensional thermal and radiation parameters

Subscripts

ent	=	entrainment
g	=	gas
l	=	liquid
o	=	oxidizer
s	=	solid
v	=	vaporization

Received 2 February 1999; revision received 8 January 2002; accepted for publication 10 January 2002.

*Research Associate, Department of Aeronautics and Astronautics. Member AIAA.
†Consulting Professor, Department of Aeronautics and Astronautics. Associate Fellow AIAA.
‡Professor, Department of Aeronautics and Astronautics. Member AIAA.

Introduction

DESPITE their safety and cost advantages over solid and liquid systems, conventional hybrid rockets possess one very significant shortcoming: very low fuel regression rates. This leads to poor fuel loading, low thrust densities, and complex grain design with multiple fuel ports, resulting in larger residuals and compromised grain integrity. The limit on regression rate for the conventional hybrid combustion configuration is set by the physical phenomena of heat and mass transfer from the relatively remote flame zone to the fuel surface.[1] As a consequence, the regression rates of modern hybrids that utilize polymers as the fuel are much lower than conventional solid-rocket burning rates.

Various methods for increasing fuel regression rates have been suggested in the past. One obvious method is to reduce the effective heat of gasification of the selected fuel. However, this approach has limited effectiveness because the variation of the effective heat of gasification is small over the range of feasible fuel types, and the increased surface blowing further limits its utility. A much more effective method is to use propellants that form a melt layer at the combustion surface. These are usually nonpolymerized substances that liquefy on heating. An obvious class includes liquids or gases at standard conditions, which are frozen to form solids (that is, solid cryogenic hybrids). Typical members of this class range from H_2, a deep cryogen, to liquid amines and hydrocarbons. However it is clear that the same internal ballistic behavior can be experienced by materials that are solids at standard conditions if they form a melt layer at the combustion surface.

Increased regression rates by several hundred percent have been observed with solid cryogenic hybrids by researchers at the Air Force Research Laboratory (AFRL)[2–4] and ORBITEC.[5,6] The AFRL program was concentrated on burning several frozen organic liquids including normal pentane with gaseous oxygen in a small test motor. On the other hand, ORBITEC tested solidified kerosene and methane with gaseous oxygen and solidified oxygen with gaseous methane (that is, a reverse hybrid configuration) using the small AFRL scale motors. In the process of developing a production technique for frozen methane fuel grains, ORBITEC conducted a limited number of tests with a low molecular weight paraffin wax. The oxidizer mass fluxes corresponding to the measured regression rates for the paraffin tests were not reported.

Initial interest on solid cryogenic hybrids was driven by performance (I_{sp}), not the regression rate. The foreseen performance improvement came from the increased number of feasible propellants that could be burned under hybrid configuration (that is, solidified O_2 and gaseous H_2). In contrast to liquid-propellant rockets, solid fuels can incorporate energetic metals to further increase performance and density. Adding metals to liquid fuels has always been a problem because of storage instability of the slurry mixture, that is, settling of metals. The resulting solid cryogenic hybrids still retain their classical advantages of nonexplosiveness, safe handling, on-off operation, simplified throttling.

The regression-rate model developed for these liquefying propellants, in addition to the classical gasification, is based on a mass-transfer mechanism resulting in the entrainment of liquid droplets from the melt layer. As will be demonstrated, droplet formation is caused by liquid layer instabilities, which result from the high velocity gas flow in the port. The purpose of this paper is to explore the development of the liquid layer at the burning surface and to determine the conditions for the onset of droplet entrainment so that its occurrence can either be invoked or avoided.

Experimental Findings

Some lab-scale cryogenic hybrid tests were performed at the Air Force Research Laboratories.[2–4] A small tube burner with a 1.14-cm inner case radius was used to investigate the performance of various frozen hydrocarbon liquids held at liquid nitrogen temperatures. These were burned with gaseous oxygen in a hybrid configuration. The primary observed variables in the tests were the chamber pressure-time history and oxidizer mass flow rate, which was held constant with use of a venturi in the oxygen feed system.[3] However, the instantaneous space-averaged regression rates, which are of primary interest in engine design, were not measured in those studies. Furthermore, the space-average regression rates were not reported by the investigators. In this section we will estimate the space-time-averaged regression rates and space-averaged instantaneous regression rates for the cryogenic tests reported in Refs. 2–4.

Table 1 Summary of data for several solid cryogenic hybrid rocket experiments performed by AFRL

Test number	Solid fuel	Nozzle area, cm^2	Burn time, s	$\dot{m}_{ox}$, g/s	Max P_c, atm	$\bar{\dot{r}}$, mm/s	$\bar{G}_o$, kg/m^2s
98	Pentane	0.206	4.5	11.4	15.0	1.48	56.2
99	Pentane	0.206	4.5	11.1	15.6	1.48	54.7
100	Pentane	0.206	4.5	11.3	15.3	1.48	55.6
101	Pentane	0.206	3.0	21.0	29.9	2.21	105.9
102	Pentane	0.100	4.5	9.9	28.6	1.48	48.8
103	Pentane	0.100	3.0	19.8	54.4	2.21	93.6
117	Pentane	0.096	4.25	10.5	30.6	1.56	51.7
118	Pentane	0.206	7.5	4.8	6.1	0.89	23.6
119	Pentane	0.206	4.25	10.4	13.6	1.56	51.2
123	Pentane	0.206	3.0	19.8	23.8	2.21	97.5
126	Pentane	0.127	5.5	7.3	15.3	1.21	35.9
127	Pentane	0.127	5.75	6.9	13.6	1.15	34.0
128	Pentane	0.127	3.80	14.3	27.2	1.75	70.4
105	2,2,5 tmh	0.093	4.75	10.2	28.9	1.40	50.3
106	HFI[a]	0.093	8.00	10.3	34.0	0.83	50.7
107	Isopropanol	0.094	9.00	10.2	28.9	0.74	50.3
108	Acetone	0.094	4.5	10.0	32.3	1.48	49.3
109	HFI	0.094	7.50	10.0	34.0	0.89	49.3
120	HFI	0.128	14.50	4.7	10.5	0.46	23.2
121	HFI	0.128	8.00	10.1	25.0	0.83	49.7

[a]HFI is a mixture of hydrocarbons: 60% isopropanol, 30% hexane, and 10% tetrahydrofuran.

For the test data shown in Table 1[2,3] for both the pentane runs and for several other fuels tested, the space-time-averaged regression rates $\bar{\dot{r}}$ can simply be calculated from the equation

$$\bar{\dot{r}} = (r_f - r_0)/t_b \tag{1}$$

Here r_0 and r_f were the same for all tests. Figure 1 shows the reduced data for the solid pentane runs in the space-time-averaged regression rate $\bar{\dot{r}}$, time-averaged oxidizer mass flux $\bar{G}_o$ plane. The averaged oxidizer mass flux is defined based on the average port radius.

$$\bar{G}_o = \frac{4\dot{m}_o}{\pi(r_0 + r_f)^2} \tag{2}$$

Regression-rate law for a typical conventional hybrid fuel, Hydroxyl Terminated Polybutadiene (HTPB), is also included in Fig. 1 for comparison purposes. A typical regression-rate expression for an HTPB-O_2 hybrid,[7] $\dot{r} = 0.025G_o^{0.65}$ mm/s where G_o is in kg/m^2-s (grain length = 15 cm), is used in the calculations. As shown in Fig. 1, the regression rates for the cryogenic pentane are 3–4 times larger than the reported regression rates for the conventional fuel, HTPB, under the same oxidizer mass flux condition.

To obtain estimates of the instantaneous regression rates during the burn, a mass balance analysis was made from the experimental pressure-time curves. The regression rate during a run can be estimated from the $P_c - t$ plot assuming an appropriate value for c^* efficiency and uniform burning. The steady-state mass balance in the chamber is

$$\dot{m} = \dot{m}_o + \dot{m}_f = \frac{P_c A_n c_d}{c^* \eta_c} \tag{3}$$

The calculation routine involves evaluating $\dot{m}_f$ at each time step from Eq. (3), where P_c, A_n, c^*, $\dot{m}_{ox}$, and η_c/c_d (assigned) are known. The value c^* at any given time is evaluated from the oxidizer to fuel ratio (O/F) of the motor. The total fuel burned is calculated at each time step and the port radius r is then calculated from geometry, that is, $M_f = \pi(r^2 - r_0^2)L\rho_s$. The instantaneous regression rate is then determined from $\dot{m}_f$, that is, $\dot{r} = \dot{m}_f/2\pi r L\rho_s$ at each time interval. If the total mass of fuel burned when $t = t_b$ is not right, η_c/c_d is

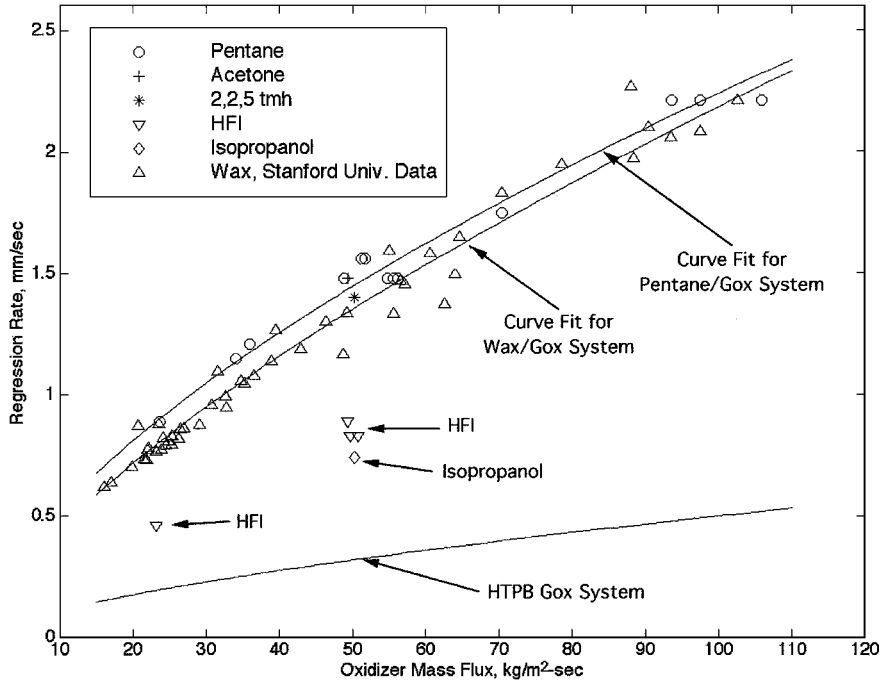

Fig. 1 Space-time-averaged regression rates are plotted vs the average oxidizer mass fluxes for various materials tested by AFRL and a specific grade of wax tested at Stanford University. Curve fit expression for pentane and wax data are $\dot{r} = 0.123\, G_o^{0.63}$ and $\dot{r} = 0.091\, G_o^{0.69}$, respectively. For comparison purposes the burning law of a classical propellant, HTPB, is included in the plot.

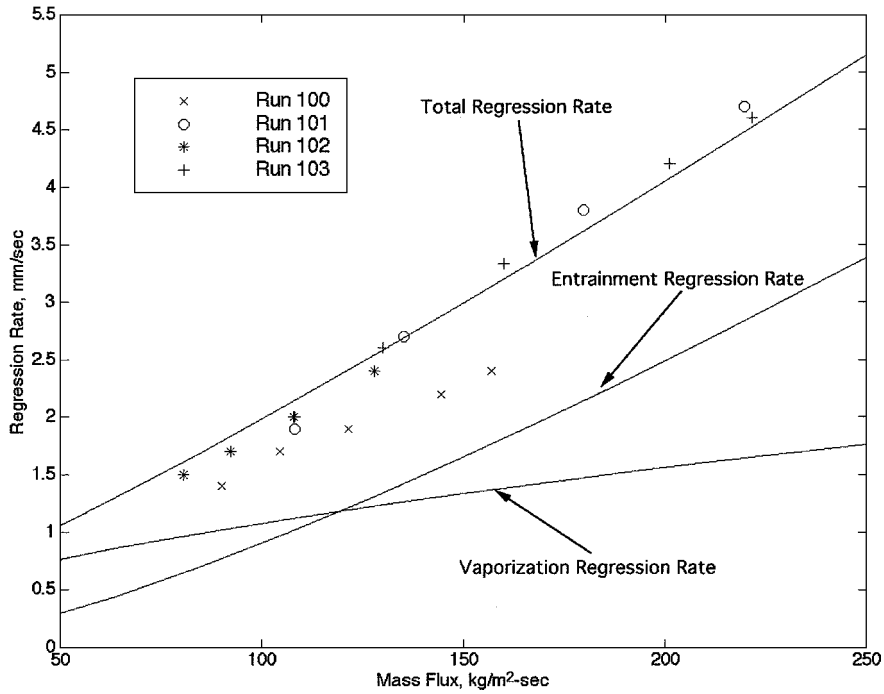

Fig. 2 Estimates of instantaneous regression rates and corresponding mass fluxes evaluated of midpoint of the port for four different pentane tests is plotted. Liquid layer theory predictions for the vaporization, entrainment, and total regression rates are included in the plot.

adjusted and the calculation routine repeated until the proper M_f is obtained. Details of this estimation technique are given in Ref. 8.

In the calculations the value of η_c/c_d was in the range of 0.9 ± 0.02. With the reported c_d value of 0.9, the resulting c^* efficiency was about 80%. This efficiency is reasonable for small motors because the chamber residence times are too short to permit complete evaporation and combustion of fuel droplets and also heat-transfer losses are significant. The reduced data for the cryogenic tests indicate that the instantaneous space-averaged regression rate reaches a maximum at about one-third of the test and drops very rapidly at the last third of the burn. The reported $P_c - t$ curves for the cryogenic pentane tests showed ignition transient times of about one-third of the total burn time. In attempting to obtain a steady-state regression-rate law, it was found that the middle third of the run gave a reasonable representation, but the latter third showed regression rates dropping rapidly, consistent with the observation of the authors.[2,3] A summary of the regression-rate values calculated for the middle third of pentane tests 100–103 is shown in Fig. 2. Regression-rate data for different tests other than test 100 collapse on a single line, confirming the validity of the data-reduction

technique. Test 100, which was performed at a distinctly lower pressure level compared to the other tests, yielded lower values for the regression rate.

We can conclude from these various experiments that the regression rates for cryogenic propellants are many times higher than for conventional hybrids. This observation cannot be explained by a lower heat of vaporization, which is insufficient to account for the regression-rate increase. Recall that in the classical regression-rate expression[9] the heat of vaporization is incorporated in the blowing parameter B raised to a power 0.32. We have estimated a maximum B value of 13.5 for pentane-O_2 system using the expressions given in Ref. 1, which would only cause a minor increase in the regression rate (30–50%) over the conventional systems rather than the observed increases of 300–400%. A different mechanism is clearly indicated, and liquid entrainment is suggested.

Development of the Theory

In this section we will develop a theory that can be used to explain the phenomena observed in the cryogenic hybrids and that will extend the applicability of the hybrid combustion theory to the fuels that can form a reasonably thick liquid layer during their combustion. Because of the complexity of the problem, we will perform the development in three stages. In the first stage we will investigate the requirements for the formation of a melt layer on the fuel grain. In the second stage we will consider the linear stability of a melt layer under the strong shear of a gas flow.[8,10] The linear stability model discussed in Ref. 10 includes the effect of the injection of liquid at the liquid-solid interface caused by the regression of the fuel slab. Later in this stage the linear stability results will be linked to the entrainment of liquid droplets with use of some experimental results and some semi-empirical relations developed in the literature. Eventually in the final stage the classical theory will be extended to the case of liquid droplet entrainment. It is shown that the primary effect of the entrainment mass transfer is to increase the regression rate of the fuel without materially increasing the thermochemically defined blowing parameter. The thermochemical blowing parameter can only be altered, to some degree, by changing the thermochemical properties of the propellants or the combustion parameters such as the local flame O/F ratio.

Thickness of the Melt Layer—Thermal Analysis

In this section the film thickness formed on a burning slab under the combined heating of convection and radiation is considered. Physically, the thickness of the liquid layer is determined by the energy transfer relations both in the solid and also in the liquid. The schematic of our thermal model for the slab configuration is shown in Fig. 3. In this investigation we are solely interested in the steady-state regression of the fuel slab. For that reason in the formulation the velocity of the liquid-gas interface and the solid-liquid interface are assumed to be equal and constant. This, of course, implies that the thickness of the melt layer is also constant. For the sake of simplicity, we further assume that the thermophysical properties of the material both in the liquid phase and also in the solid phase are uniform. The effect of convection in the liquid layer is also ignored because of the small melt layer thicknesses for which the Reynolds numbers are relatively small (a couple of hundreds) and the temperature gradients are fairly large.

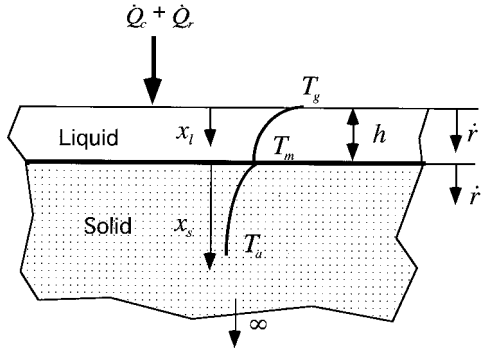

Fig. 3 Schematic of the thermal model used in the melt layer thickness estimation.

In the analysis the possibility of the penetration of the thermal radiation into the slab is considered. Several simplifying assumptions are introduced in our radiation treatment. First, the radiative flux field is assumed to be one-dimensional. Because the temperature levels in the slab are small, the contribution of radiation emitted by internal material to the radiative intensity is negligible. The absorbing character of both the liquid and also the solid material are assumed to behave like a gray body, namely, the absorption coefficient is independent of the frequency of the radiation. The absorption characteristics for typical hydrocarbons used in cryogenic hybrid applications, such as pentane, are reasonably flat in the medium infrared (IR) range of the spectrum.[11,12] Even if this is not the case, the use of a constant absorption coefficient obtained by averaging over the band of the spectrum of the incoming radiation can be justified.[13] Furthermore, the noncollimated effects of the incoming radiation to the fuel slab surface are neglected.

Under these simplifications the radiative energy flux in the liquid and solid phases of the slab can be written as

$$q_r(x_l) = \dot{Q}_r e^{-a_l x_l}, \qquad q_r(x_s) = q_r^h e^{-a_s x_s} = \dot{Q}_r e^{-a_l h} e^{-a_s x_s} \tag{4}$$

$\dot{Q}_r$ is the total collimated radiative flux impinging on the surface. The flux is generated by the emission from the hot combustion products in the gas phase. In hybrids it is reported that the effective radiation temperatures of the gases fall in the range of 1500–2000 K (Ref. 1). The radiation levels from the gas phase are significantly elevated in the presence of solid emitting particles in the gas flow. These solid particles can either be oxidized metal additives to the solid fuel or the soot, which is a natural product of hydrocarbon combustion at fuel-rich stoichiometries.

The radiative heating of material at any position can be expressed as the divergence of the radiative flux $-\nabla \cdot \boldsymbol{q}_r$. In our one-dimensional model the radiative heating in the solid and the liquid become

$$-\frac{\mathrm{d}q_r}{\mathrm{d}x_s} = a_s \dot{Q}_r e^{-a_l h} e^{-a_s x_s}, \qquad -\frac{\mathrm{d}q_r}{\mathrm{d}x_l} = a_l \dot{Q}_r e^{-a_l x_l} \tag{5}$$

It can be shown by the following integral that the total heating of the fuel by radiation matches the radiative heat input:

$$\int_0^h a_l \dot{Q}_r e^{-a_l x_l}\,\mathrm{d}x_l + \int_0^\infty a_s \dot{Q}_r e^{-a_l h} e^{-a_s x_s}\,\mathrm{d}x_s = \dot{Q}_r \tag{6}$$

We will now consider the energy equations in the liquid and in the solid phases. The field equation in the liquid phase deserves special attention. Because of the density difference between solid and liquid phases, the liquid particles in the melt layer possess a nonzero vertical velocity in the laboratory frame of reference. The expression for that vertical velocity component, which can be readily obtained from a mass balance argument across the liquid-solid interface, can be written as $v_l = (\rho_s/\rho_l - 1)\dot{r}$. Here v_l is the vertical velocity of the liquid in the laboratory frame of reference. Consequently, in a reference frame that moves with the regressing surface the net liquid velocity becomes $(\rho_s/\rho_l)\dot{r}$, as compared to the solid velocity of $\dot{r}$.

In light of the preceding arguments, the liquid layer energy equation can be written as

$$\frac{\mathrm{d}^2T}{\mathrm{d}x_l^2} + \frac{1}{\delta_l}\frac{\mathrm{d}T}{\mathrm{d}x_l} = -\frac{a_l \dot{Q}_r}{\kappa_l \rho_l C_l} e^{-a_l x_l} \tag{7}$$

where the characteristic thermal thickness in the liquid phase is defined as $\delta_l = \kappa_l \rho_l / \dot{r} \rho_s$.

The general solution for this linear ordinary differential equation can be found as

$$T(x_l) = c_1 e^{-x_l/\delta_l} + c_2 - \frac{\dot{Q}_r}{\rho_l C_l \dot{r}(a_l\delta_l - 1)} e^{-a_l x_l} \tag{8}$$

For boundary conditions $T(0) = T_v$ and $T(h) = T_m$, the temperature gradients at the two boundaries can be determined as

$$\left.\frac{dT}{dx_l}\right|_{x_l=0} = \frac{1}{\delta_l}\left(-\frac{\Delta T_1}{1-\phi} + \frac{1-\varphi}{1-\phi}A_l - R_l A_l\right) \tag{9}$$

$$\left.\frac{dT}{dx_l}\right|_{x_l=h} = \frac{1}{\delta_l}\left[-\frac{\phi}{1-\phi}\Delta T_1 + \frac{\phi}{1-\phi}(1-\varphi)A_l - \varphi R_l A_l\right] \tag{10}$$

The parameters that appear in these expressions are $\Delta T_1 = T_v - T_m$, $R_l = a_l\delta_l$, $\phi = e^{-h/\delta_l}$, $\varphi = e^{-a_l h}$ and $A_l = -\dot{Q}_r/\rho_l C_l \dot{r}[1/(a_l\delta_l - 1)]$.

Next, a similar treatment is performed for the solid phase. The energy equation in the solid is

$$\frac{d^2T}{dx_s^2} + \frac{1}{\delta_s}\frac{dT}{dx_s} = -\frac{a_s \dot{Q}_r}{\kappa_s \rho_s C_s} e^{-a_s x_s} \tag{11}$$

where the thermal thickness in the solid is defined as $\delta_s = \kappa_s/\dot{r}$. All other parameters are defined as their liquid-phase analogs. Similarly, the general solution for the solid phase is

$$T(x_s) = c_1 e^{-x_s/\delta_s} + c_2 - \frac{\dot{Q}_r \varphi}{\rho_s C_s \dot{r}(a_s\delta_s - 1)} e^{-a_s x_s} \tag{12}$$

The temperature gradient at the liquid-solid interface can easily be determined upon the application of the boundary conditions $T(0) = T_m$ and $T(\infty) = T_a$.

$$\left.\frac{dT}{dx_s}\right|_{x_s=0} = \frac{1}{\delta_s}(-\Delta T_2 - A_s R_s + A_s)$$

The recently introduced parameters are $\Delta T_2 = T_m - T_a$, $R_s = a_s\delta_s$, and $A_s = -\dot{Q}_r\varphi/\rho_s C_s \dot{r}[1/(a_s\delta_s - 1)]$. T_a is the ambient temperature of the solid fuel grain.

Now we will consider the energy balance at the liquid-solid interface. Namely, the energy transfer from the liquid to the interface must be equal to the heat conducted into the solid from the interface and the energy required for the phase transformation. In mathematical terms this can be expressed as

$$-\lambda_l \left.\frac{dT}{dx_l}\right|_{x_l=h} + \lambda_s \left.\frac{dT}{dx_s}\right|_{x_s=0} - L_m \rho_s \dot{r} = 0 \tag{13}$$

Here L_m is the heat of fusion for the fuel material of interest.

The temperature derivative expressions already derived can be inserted in this energy balance formula. After several simplifications one obtains the following relation between the variables ϕ and φ.

$$\phi = \frac{h_m \rho_s \dot{r}(R_l - 1) + \dot{Q}_r \varphi}{h_e \rho_s \dot{r}(R_l - 1) + \dot{Q}_r} \tag{14}$$

Here the following definitions of total effective heats are introduced for simplicity:

$$h_m = L_m + C_s \Delta T_2 \tag{15a}$$

$$h_e = h_m + C_l \Delta T_1 \tag{15b}$$

From a practical point of view, it is desirable to replace the regression rates appearing in this expression with a commonly used parameter, the total effective heat of gasification. We will further follow the energy considerations to derive a relation for the effective heat of gasification.

The energy balance at the liquid-gas interface requires that the convective heat transfer from the gas to the interface must be equal to the conductive heat transfer into the liquid and the heat required for the phase transformation, namely,

$$\dot{Q}_c + \lambda_l \left.\frac{dT}{dx_l}\right|_{x_l=0} - L_v \rho_s \dot{r}_v = 0 \tag{16}$$

In this formula we allowed for the possibility of entrainment mass transfer from the liquid surface other than the mass transfer by vaporization. This feature is, in fact, the basis of our liquid layer combustion theory. Thus $\dot{r}_v$, which appears in the energy balance expression, represents the evaporative contribution to the total regression rate because only the evaporative mass transfer contributes to the thermal energy balance.

Next we add the energy balance equations at the liquid-solid and gas-liquid interfaces together. The final result of this operation is simply

$$\dot{Q}_w = \dot{Q}_c + \dot{Q}_r = h_e \rho_s \dot{r} + L_v \rho_s \dot{r}_v \tag{17}$$

This can be interpreted as follows: the total energy transferred from the surroundings must be equal to the total energy absorbed in the slab, which is composed of the energy required to heat the liquid and solid and the heat required for the phase transformations.

Now with the use of Eq. (17), we define the effective heat of gasification as it is commonly used in the hybrid literature:

$$h_v \equiv \dot{Q}_w/\rho_s\dot{r} = C_l\Delta T_1 + C_s\Delta T_2 + L_m + L_v(\dot{r}_v/\dot{r}) \tag{18}$$

The form of Eq. (18) is different than the expressions commonly given in the literature because the heat required to vaporize the material transported by means of entrainment is zero.

Eventually, note that the variables ϕ and φ are related according to the simple relation $\varphi = \phi^{R_l}$. After combining Eqs. (14) and (18), we obtain a nonlinear equation for the thickness parameter $\phi = e^{-h/\delta_l}$:

$$\phi = \frac{h_m(R_l - 1) + h_v(\dot{Q}_r/\dot{Q}_w)\phi^{R_l}}{h_e(R_l - 1) + h_v(\dot{Q}_r/\dot{Q}_w)} \tag{19}$$

Note that

$$\frac{\dot{Q}_r}{\dot{Q}_w} = \frac{\dot{Q}_r/\dot{Q}_c}{1 + \dot{Q}_r/\dot{Q}_c}$$

An interesting observation is that R_s does not appear in Eq. (19) and the melt layer thickness is independent of the absorptivity of the solid material. This can be explained from the fact that the only contribution of the solid-state temperature distribution on the thickness is through the heat transfer from the solid at the liquid-solid interface [Eq. (13)]. It can be shown that the solid thermal profile in the neighborhood of the interface and thus the heat flux at the interface (from the solid side) is independent of the distribution of the radiative heating in the solid (or R_s).

An explicit solution for this algebraic nonlinear equation, [Eq. (19)] for the general case could not be attained. We focus on the following two limiting cases of practical interest. R_l is the ratio of the thermal thickness to the radiative penetration thickness in the liquid layer.

1) $R_l \gg 1$: The absorption of the radiation in the liquid layer is very large. In this extreme case of an opaque liquid layer, all of the radiative heat is absorbed at the liquid-gas interface. The thickness can be solved explicitly as

$$h = \delta_l \ln(1 + C_l\Delta T_1/h_m) \tag{20}$$

where the characteristic thermal thickness of the liquid layer is $\delta_l = \kappa_l\rho_l/\dot{r}\rho_s$. All of the thermophysical properties of the fuel material are lumped in the logarithmic term, and the $\dot{Q}_r/\dot{Q}_c$ ratio does not affect the thickness. This case is important for propellants that are loaded with strongly absorbing materials such as carbon black.

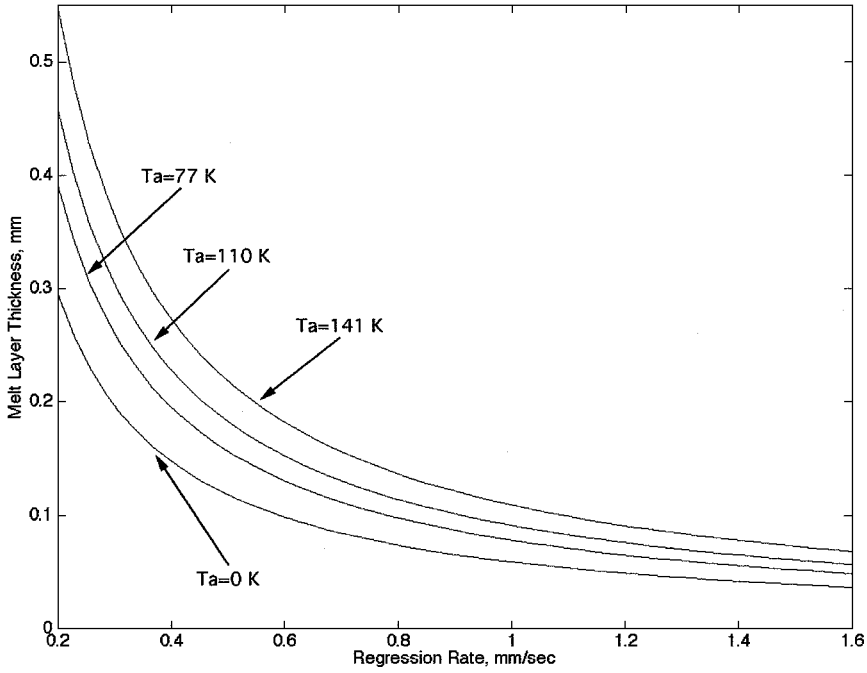

Fig. 4 Effect of regression rate and initial slab temperature on the melt layer thickness for pentane.

2) $R_l \ll 1$: In this other extreme, the absorption of the radiation in the liquid phase is small. Here the thickness of the thermal layer in the liquid is much smaller than the radiative thickness in the liquid, and as a consequence all of the radiative flux is absorbed in the solid. The effect of the entrainment mass transfer on the thickness is also included in this formulation. Unlike the other extreme, in this case the film thickness depends on the ratio of the radiative heat flux to the convective heat flux, and it can be expressed as

$$h = \delta_l \ell n\left[1 + \frac{C_l \Delta T_1}{h_m - h_v(\dot{Q}_r/\dot{Q}_w)}\right] \tag{21}$$

The dependence of the thickness on $\dot{r}_v/\dot{r}$ comes from the effective heat of gasification h_v that appears explicitly in this formula and is defined in Eq. (18). An important common property of the regression-rate expressions [Eqs. (20) and (21)] is that the melt layer thickness is proportional to the characteristic thermal length of the liquid δ_l and thus inversely proportional to the regression rate ($h \propto 1/\dot{r}$).

As indicated by Eq. (19), some knowledge of the order of magnitude of the liquid absorptivity parameter is essential for a reliable estimation of the melt layer thickness. We have calculated the average absorptivity of n-pentane using the published near-infrared region (NIR) and middle-infrared region absorption spectra for this material.[11,12] In the calculations we have assumed a continuous spectral distribution (according to Planck's law) for the intensity of the impinging radiation from the combustion gases at an effective radiation temperature of 1800 K. At this temperature the radiation peak takes place at a wave number of 6211 cm^{-1}, and most of the heat transfer is in the NIR of the spectrum. The estimated average absorption coefficient for pentane is $a_l = 1.62$ mm^{-1}, which results in $R_l = 0.13/\dot{r}$ (that is, $\dot{r}$ is in millimeters/second). For pure pentane at regression-rate values larger than 1 mm/s, which are typical for fast-burning liquefying propellants, the liquid absoptivity can be ignored. Thus for all pentane melt layer thickness calculations presented in this paper, the approximate relation [Eq. (21)] is used instead of the exact nonlinear relation [Eq. (19)].

One of the important parameters that affect the thickness of the melt layer is the ambient temperature of the fuel slab (which appears in ΔT_2). Figure 4 shows the plots of the melt layer thickness vs the regression rate for various ambient temperatures for a pentane fuel slab for $\dot{Q}_r/\dot{Q}_c = 0.1$ and $\dot{r}_v/\dot{r} = 0.5$. The material properties used in the calculations are given in Table 2.[14] An increase in the ambient temperature of the fuel slab results in an increase in the melt layer thickness. The maximum film thickness for a given regression rate is attained when the ambient temperature is equal to the melting temperature.

A plot of the variation of the film thickness with the relative radiative heat transfer, $\dot{Q}_r/\dot{Q}_c$, for a pentane system is shown in Fig. 5. The figure reveals the interesting phenomenon that at a critical value of the radiation factor (around 0.3 for pentane with 10% entrainment) the steady-state film thickness grows indefinitely. This fact can be seen from Eq. (21), namely, at the critical value of this factor the numerator of the argument of the logarithm diminishes. In physical terms, during this critical operation, the energy balance at the liquid-solid interface requires zero conductive heat transfer from the liquid side. This condition imposes a zero temperature gradient on the liquid side of the interface, which can only be achieved with an infinite thickness of the liquid layer. However the growth to large thicknesses can only be achieved in a long transient period, which cannot be estimated with our steady-state model. Figure 5 also shows that the effect of entrainment mass transfer is to reduce the thickness at a given radiation factor and to increase the critical value of the radiation factor. This effect is generated from the entrainment regression-rate dependence of the effective heat of gasification [Eq. (18)].

Stability of the Liquid Layer—Entrainment

The linear stability of thin films under strong blowing is studied in Ref. 10. It is shown that the layer can be unstable over a wide range of parameters. Now this observation needs to be related to the entrainment phenomenon of the liquid droplets into the gas stream. The rigorous treatment of the entrainment problem requires a fully nonlinear investigation. In this study we avoid this difficulty by developing empirical relations for the entrainment with use of some experimental data and the linear stability results.

The most relevant experimental work on entrainment is reported by Gater and L'Ecuyer in an early paper.[15] In this study the entrainment rates from thin films of various liquids (including some hydrocarbons such as RP-1, methanol) under strong gas flow were measured. The experiments were performed in a wind tunnel, and some tests were executed with hot gas flow. The most significant result of this study is that the entrainment mass transfer per unit area $\dot{m}_{\text{ent}}$ is proportional to the mass flow rate per unit width of the

Table 2 Material properties of the propellants used in the calculations (Ref. 14)[a]

Propellant	Pentane C_5H_{12}	Acetone C_3H_6O	2,2,5 tmh C_9H_{20}	Wax	Oxygen O_2	HFI	Isopropanol C_3H_8O
Molecular weight, g/mol	72.15	58.08	128.26	432.8	32.0	69.11	60.10
Heat of formation, kJ/mol	−146.8	−217.2	−254.0	−697.2	0.0	−231.7	−272.4
Surface tension, mN/m	14.3	19.2	11.3	7.1	13.2	15.6	16.4
Viscosity, mPa-s	0.46	0.51	0.42	0.65	0.33	2.5	5.0
Density-liquid phase, kg/m^3	688.4	835.2	719.8	654.4	1226.9	785.0	808.9
Melting temperature, K	143.3	178.45	167.4	339.6	54.4	181	183.3
Boiling temperature, K	309.6	329.44	397.2	727.4	90.2	350	355.4
Heat of fusion, kJ/kg	116.7	98.0	48.3	167.2	13.7	96.3	89.4
Heat of vaporization, kJ/kg	357.8	513.0	261.8	163.5	190.58	540.2	663.4
Thermal conductivity—liquid phase, W/mK	0.14	0.17	0.12	0.12	0.17	0.137	0.14
Specific heat—liquid phase, kJ/kg-K	2.06	2.07	2.00	2.92	1.67	2.03	2.28
Specific heat—solid phase, kJ/kg-K	1.10	1.33	——	2.03	0.83	1.09	1.10
Entrainment parameter, relative to pentane	1	0.73	1.29	0.86	1.48	0.17	0.08
Burning-rate characteristic	High	High	High	High	High	Low	Low

[a]Liquid properties other than surface tension are evaluated at a mean temperature between the melting and vaporization temperatures. Surface tension is evaluated at the boiling temperature. (See Ref. 8 for the estimation of properties for the mixtures HFI and wax.)

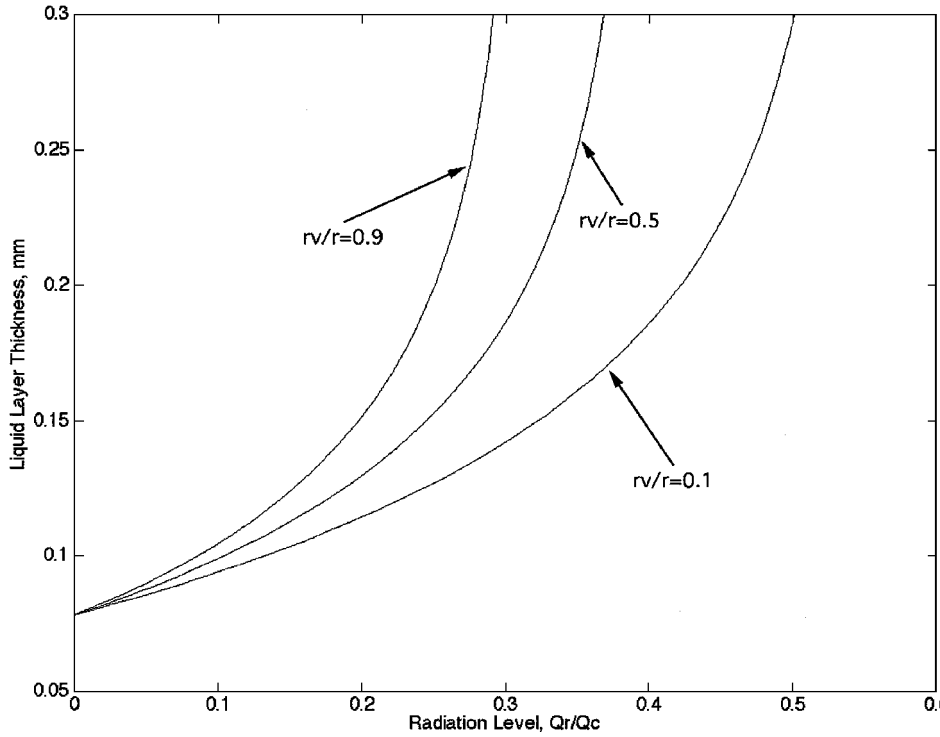

Fig. 5 Effect of radiative heat transfer on the melt layer thickness of a pentane slab for various vaporization rates are plotted. The plots are for regression rate of 1 mm/s and initial slab temperature of 77 K.

wind-tunnel test section $\dot{m}_l$. The dimensional proportionality function $e_0(X_e)$ is formulated in terms of the dynamic pressure of the gas flow P_d, surface tension σ, and a temperature ratio according to the following simple formula:

$$\dot{m}_{\text{ent}} = 13.3\, e_0(X_e)\dot{m}_l \qquad \text{where} \qquad X_e = P_d^{0.5} \Big/ \sigma (T_g/T_v)^{0.25} \tag{22}$$

The temperature ratio is included as a correction for the density variation in the gas. The following empirical formula for the proportionality function $e_0(X_e)$ can be used to calculate the entrainment mass transfer per unit area of liquid surface $\dot{m}_{\text{ent}}$ in kilograms/square meter-second for a given mass flow rate per unit width of the liquid $\dot{m}_l$ in units of kilograms/meter-second.

$$e_0(X_e) = 1 - \exp\left[-1.06 \times 10^{-4}(X_e - 2109)\right] \tag{23}$$

In this relation the units of X_e is Newtons$^{-1/2}$. With use of the shear force balance at the liquid gas interface ($c_f P_d = \mu_l u_l / h$), the liquid mass flow rate within the melt layer per unit width can easily be related to the properties of the gas flow and liquid film under consideration.

$$\dot{m}_l = \frac{P_d c_f h^2 \rho_l}{2\mu_l} \tag{24}$$

Equation (22) for the entrainment mass transfer ignores the effect of reduction in the liquid mass flow rate along the axial direction. In the experiments that were conducted to obtain Eq. (22), there is no liquid injection along the axis.[15] This might be a significant source of error at high mass transfer rates for which the decrease of the film thickness is important. For that reason we modify the entrainment expression to correct for this effect. The modified entrainment mass transfer rate becomes

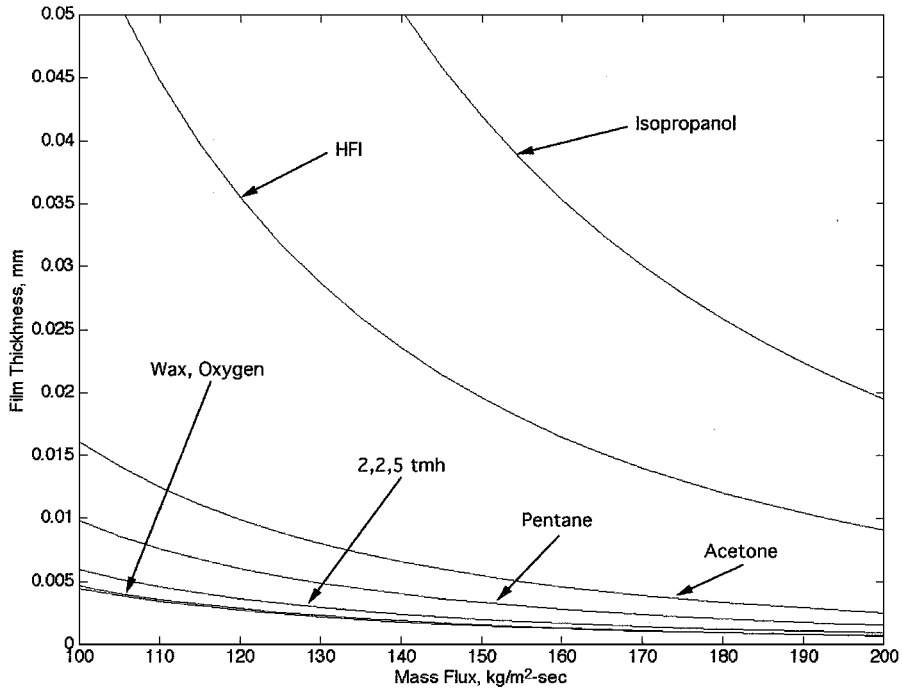

Fig. 6 Entrainment onset boundaries in the thickness mass flux plane for various propellants are plotted. Equation (28) is used in the calculations.

$$\dot{m}_{\text{ent}} = -13.3\,\ell n(1 - e_0)\dot{m}_l \tag{25}$$

Upon the substitution of Eq. (23) in Eq. (25), the following expression for the entrainment mass transfer and entrainment regression rate is obtained:

$$\dot{m}_{\text{ent}} = \rho_l \dot{r}_{\text{ent}} = 1.41 \times 10^{-3}(X_e - 2109)\dot{m}_l \tag{26}$$

This relation or the original expression, Eq. (22) is only valid for $X_e > 2109$ ($N^{-1/2}$). Namely, if the entrainment parameter is less than the critical value there is no entrainment mass transfer from the film.

After the preceding correction the entrainment mass transfer becomes proportional to a difference between the entrainment parameter X_e and its critical value at the onset of entrainment. This is a form commonly found in the literature.[16] For hybrid applications with sufficiently large X_e, the entrainment mass transfer is approximately proportional to $P_d^{3/2}$.

The empirical result just stated is in good qualitative agreement with the linear stability theory predictions from Ref. 10. First, the entrainment increases monotonically with the entrainment parameter. Thus similar to the linear stability, the gas dynamic pressure is destabilizing, and the surface tension and viscosity are stabilizing. Moreover, below a critical level of the entrainment parameter there is no entrainment observed. This is also consistent with the requirement for the interface disturbance to posses a minimum amplification rate to yield any entrainment.

In the nuclear reactor field there has been significant research on the entrainment mass transfer[16,17] because it has importance in the emergency cooling of the reactors. Various models for entrainment are developed at various regimes of operation. At high Reynolds numbers, which are more relevant to our case, a roll wave mechanism for the liquid entrainment is suggested.[17] In general, the experimental findings of those studies also confirm the results already mentioned. However the form of dependence of the entrainment mass transfer on the parameters is somewhat different in every study. Thus it is fair to state that the proper form of scaling for the entrainment still needs to be resolved.

In the light of experimental findings and the results of the linear theory, we suggest the following general empirical expression (for operation sufficiently remote from the critical conditions for entrainment) for the entrainment rate of liquid droplets in terms of the relevant properties of the hybrid motor:

$$\dot{m}_{\text{ent}} \propto P_d^{\alpha} h^{\beta} \Big/ \mu_l^{\gamma} \sigma^{\pi} \tag{27}$$

The experimental curve fits and the linear stability theory suggest that the dynamic pressure exponent is in the range of 1–1.5. For example, Gater and L'Ecuyer[15] scaling for large mass fluxes indicates that α is approximately 1.5 and β is equal to 2. The viscosity and surface tension exponents are both predicted to be 1. The series of entrainment relations given by Nigmatulin et al.[16] suggest a weaker dependence on both the dynamic pressure and also the thickness ($\alpha = 1$ and $\beta = 1$). The scaling with respect to the material properties is not estimated accurately by the entrainment relations given by Nigmatulin because mainly water data were considered in the study. We believe that under the conditions of hybrid rocket applications, the melt layer viscosity plays a more important role compared to the surface tension in establishing the entrainment mass transfer rate (that is, $\gamma > \pi$).

A very useful empirical relation for the critical conditions for the onset of entrainment given by Ref. 18 is rearranged here in terms of the practical conditions in the motor:

$$G^{1.6} h^{0.6} \geq 2.5 \times 10^{-3} \frac{1}{c_f^{0.8}} \frac{\rho_g^{1.3}}{\rho_l^{0.3}} \frac{\mu_l^{0.6} \sigma}{\mu_g} \tag{28}$$

This relation only holds for a laminar film ($Re < 300$). Unlike the entrainment relations this formula has the correct scaling with the material properties of the liquid. Figure 6 shows the plot of the entrainment boundary for various liquid materials in the mass flux film thickness plane (see Table 2 for the material properties used in calculations). For each liquid the entrainment takes place in the region above the curve.

Extended Hybrid Theory

It has been shown in the preceding sections that a liquid layer can be formed on the fuel grain and this liquid layer can be unstable over a reasonable range of parameters typical of hybrid operation. It is also indicated that the instabilities in the liquid layer can enhance the entrainment of liquid droplets into the gas stream. The final phase of the development involves the modification of the classical hybrid boundary-layer combustion theory for the possibility of the entrainment mass transfer from the fuel grain.

The formation of the liquid layer instabilities and entrainment of liquid droplets require three major modifications in the classical hybrid combustion theory:

1) The ratio of the enthalpy difference to the effective heat of gasification ($\Delta h/h_v$) that appears in the thermal blowing parameter expression is altered. The effective heat of gasification is reduced because the evaporation energy required for the fuel mass transfer from the surface is partly avoided by the mechanical entrainment of the liquid, whereas the enthalpy difference between the flame and the surface is also reduced because some of the reactants are now in liquid phase. It is estimated that the reduction in the effective heat of gasification is more dominant than the change in the enthalpy difference. Thus, as a first approximation we assume that the reduction in the flame enthalpy is negligible.

2) The blocking factor C_H/C_{H0} that modifies the convective heat flux to the surface is also altered as a result of the presence of the two-phase flow. As a first approximation, we ignore the effect of the liquid droplets on the momentum and energy transfer. Under this assumption the blocking factor can be expressed as a function of evaporation blowing parameter:

$$C_H/C_{H0} = f(B_g)$$

The evaporation blowing parameter B_g includes only the gaseous phase mass transfer from the fuel surface. We assume that evaporation of the droplets released from the liquid surface into the gas stream does not take place beneath the flame sheet. This assumption is consistent with the flame sheet approximation, which is a standard one in hybrid combustion modeling. Moreover, it is a reasonable approximation for typical hybrid operating conditions that are characterized by high blowing rates and thus low residence time of droplets between the liquid surface and the diffusion flame. However, we believe that a more rigorous treatment of the two-phase flow in the hybrid boundary layer will be an important step in the further improvement of the liquefying hybrid theory.

3) The ripples formed on the liquid layer surface increase the surface roughness and the heat transfer from the flame front to the surface.

In general, the total regression rate of a hybrid motor can be written as a sum of the evaporation regression rate that is generated by the vaporization of the liquid into the gas stream and the entrainment regression rate that is related to the mass transfer mechanically extracted from the liquid surface.

$$\dot{r} = \dot{r}_v + \dot{r}_{\text{ent}} \tag{29}$$

For an arbitrary combination of the entrainment and evaporative mass transfer, the energy balance at the liquid gas interface is

$$\dot{r}_v + \left[R_{\text{he}} + R_{\text{hv}}\left(\frac{\dot{r}_v}{\dot{r}}\right)\right]\dot{r}_{\text{ent}} = F_r \frac{0.03\mu_g^{0.2}}{\rho_f}\left(1 + \frac{\dot{Q}_r}{\dot{Q}_c}\right) B \frac{C_H}{C_{H0}} G^{0.8} z^{-0.2} \tag{30}$$

where

$$R_{\text{hv}} = \frac{C_l \Delta T_1}{h_e + L_v}, \qquad R_{\text{he}} = \frac{h_m}{h_e + L_v} \tag{31}$$

Here the nondimesional energy parameters for entrainment R_{he} and vaporization R_{hv} are introduced because the material that is extracted through the entrainment mechanism possesses different heating histories (that is, no heat of vaporization is required for entrainment). We postulate that the effective heating in the liquid phase required for fuel material, which is going through the entrainment mass transfer mechanism, reduces linearly as the vaporization component of the regression rate decreases. This extra complexity, which was ignored in the thickness estimation arguments, is introduced to capture the asymptotic behavior of regression rate in the entrainment-dominated region of operation. The effect of reduced liquid-phase heating on the thickness at moderate entrainment conditions is very small because the thickness presents a logarithmic dependence on the energy terms.

The roughness parameter F_r is introduced in the energy equation to account for the increased heat transfer by wrinkling of the liquid surface. It has been argued by Gater and L'Ecuyer[14] that the surface roughness decreases with increasing dynamic pressure of the gas flow. This argument is based on the observed reduction in the scale of the interface disturbances with increasing dynamic pressure. This phenomenon is confirmed by the linear theory.[10] The empirical formula for the roughness correction parameter suggested by Gater and L'Ecuyer can be expressed in terms of the operational parameters of the motor as

$$F_r = 1 + \frac{14.1\rho_g^{0.4}}{G^{0.8}(T_g/T_v)^{0.2}} \tag{32}$$

We developed a new curve fit expression for the blowing correction C_H/C_{H0}, which is a reasonable approximation for the analytical expression given by Marxman[19] for a wide B_g range of 0–14 (see Fig. 7).

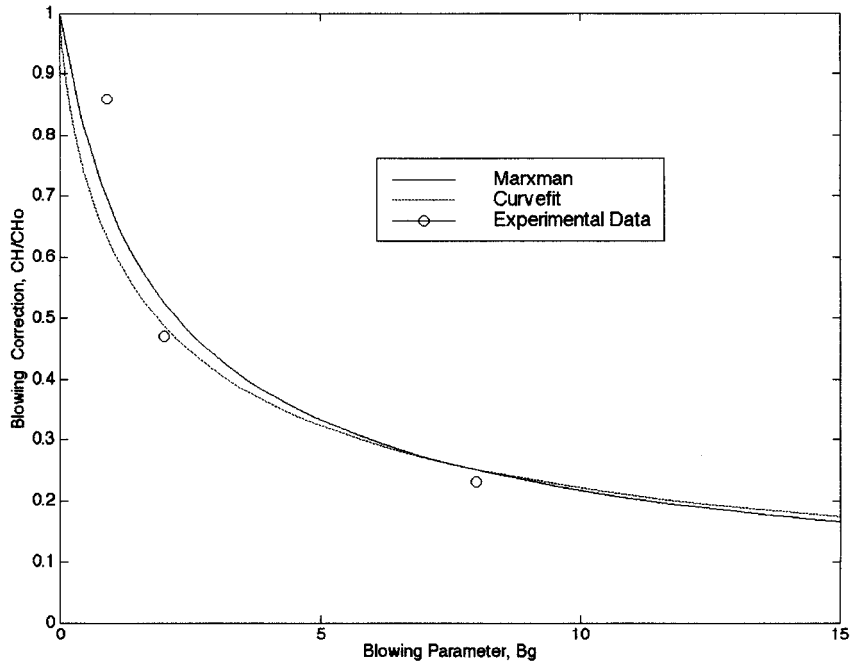

Fig. 7 Blowing corrections according to Marxman's formula and our curve fit expression, Eq. (33), are plotted as a function of the blowing parameter. The experimental points are reported in Ref. 19.

$$\frac{C_H}{C_{H0}} \cong \frac{2}{2+1.25B_g^{0.75}} = \frac{C_{B1}}{C_{B1}+C_{B2}(\dot{r}_v/\dot{r}_{\rm cl})^{0.75}} \tag{33}$$

Here the coefficients are defined as

$$C_{B1} \equiv \frac{2}{2+1.25B^{0.75}}, \qquad C_{B2} \equiv \frac{1.25B^{0.75}}{2+1.25B^{0.75}}$$

It is not acceptable to adapt one of the forms that are commonly used in the hybrid literature[1,9] (that is, $B^{-0.68}$) in this study in which accuracy at low B values is essential. Classical expressions predict unrealistically large blocking factors (even larger than one) for B values close to zero. The classical regression rate can be written as

$$\dot{r}_{\rm cl} = \frac{0.03\mu_g^{0.2}}{\rho_f}\left(1+\frac{\dot{Q}_r}{\dot{Q}_c}\right)BC_{B1}G^{0.8}z^{-0.2} \tag{34}$$

Following the proceeding section's arguments [Eq. (27)], the entrainment regression rate can be written in terms of the mass flux in the port and the total regression rate:

$$\dot{r}_{\rm ent} = a_{\rm ent}(G^{2\alpha}/\dot{r}^{\beta}) \tag{35}$$

Here we used the definition of the dynamic pressure ($P_d = G^2/2\rho_g$) and Eqs. (20) or (21) for the film thickness expression. The coefficient $a_{\rm ent}$ is a function of the properties of the selected propellant and average gas density ρ_g in the chamber. For simplicity we will assume that is a constant for a given propellant.

Equations (29–32) and (35) together with the blowing correction expression, Eq. (33), form a nonlinear set of algebraic equations that can be solved for a given propellant combination to obtain the total regression rate as a function of the axial location and local mass flux. For pentane as the frozen fuel, the regression rates are calculated iteratively from this nonlinear set of equations as a function of the mean mass flux in the port. Figure 2 shows both the estimated regression rates and also the reduced data for the pentane runs. In the calculations $\alpha = 1.5$, $\beta = 1.5$, $a_{\rm ent} = 8 \times 10^{-14}$ ($\rm m^{8.5}s^{0.5}/kg^3$), $\dot{Q}_r/\dot{Q}_c = 0.15$, $z = L/2 = 0.075$ m, $\rho_g =$ 4 kg/m^3, and $\mu_g = 6.5 \times 10^{-5}$ N-s/m^2 numerical values are used. The estimated blowing parameter value of 13.5 for the pentane-oxygen system is used in the calculations. The figure shows that the high regression rates observed in the pentane tests can be explained in the context of the liquid layer combustion theory. Most of the increase in the burning rate comes from the entrainment of droplets: reduced effective heat of gasification and reduced blocking correction. The roughness effect, however, accounts for a smaller increase in regression rates (that is, increase in the surface heat-transfer ranges from 30% at low mass fluxes down to 5% at the higher flux levels).

It is useful to obtain an upper limit for the regression rate of a hybrid fuel forming a liquid layer. In the extreme case the vaporization from the liquid surface is negligible, namely, all of the mass is transferred to the gas flow in form of droplets. This upper bound can be quantitatively determined upon the consideration of Eq. (30). The maximum regression rate occurs when no vaporization at the surface takes place. Under the assumptions of our theory, for this extreme case the blocking factor becomes unity. The maximum regression rate normalized with the classical value of the regression rate, for which no entrainment from the surface is allowed, becomes

$$\dot{r}_{\rm max}/\dot{r}_{\rm cl} = 1/C_{B1}R_{\rm he} \tag{36}$$

For pentane fuel the maximum regression rate is estimated to be approximately 20 times the classical regression rate. For pentane calculations the blowing parameter value of 13.5 and $R_{\rm he}$ value of about 0.25 are used. This large upper limit for the amplification explains the experimentally observed regression rates that are determined to be 2–5 times larger than the expected (classical) values.

As shown in Table 1 and Fig. 1, some hydrocarbons such as pentane, acetone, and 2, 2, 5 tmh burn fast, whereas some others such as isopropanol and Hexane Tetrahydrofuran Isopropanol (HFI) burn considerably more slowly. This observation can also be explained within the context of the liquid layer hybrid theory developed in this section. Figure 6 shows the entrainment onset boundary for various propellants generated with use of Eq. (28). The parameter values of $\rho_g =$ 4 kg/m^3, $c_f = 0.004$, and $\mu_g = 6.5 \times 10^{-5}$ N-s/m^2 are used in the calculations. It is clear that isopropanol and HFI, which are much more viscous compared to the other materials, require large thresholds for entrainment. To reinforce this finding, we have used the scaling law, Eq. (27) to estimate the entrainment rates for given mass flux and film thickness for various materials. The entrainment rates are then reduced to entrainment parameters by normalizing with the entrainment rate for the reference propellant pentane. Calculations are performed with use of the viscosity and surface tension exponents of 1 and 0.7, respectively. The relative entrainment parameters are shown in Table 2. Clearly, the entrainment parameters of the viscous propellants (that is, isopropanol, HFI) are one order of magnitude smaller than the other propellants. This finding reveals viscosity as a determining parameter controlling the burning rate of a cryogenic hybrid propellant. In fact, viscosity of the embedded propellant can be adjusted to tailor the regression rate of a cryogenic hybrid rocket during the course of its operation. Moreover it can be stated that oxygen, which is an interesting alternative solid cryogenic hybrid propellant, is also predicted to be a fast burning material because of its low viscosity. This result is confirmed by the tests performed by ORBITEC.[6]

Another important practical issue for the prediction of the performance of a propellant is its susceptivity to bulk heating by radiation penetrated through the slab. Specifically, it can be stated that the materials, which have small radiative absorptivities in their solid phases, potentially burn in an uncontrolled fashion. This is because of the possibility of sloughing of the propellant that is internally heated. To investigate this, we have estimated the outer web temperature as a function of the remaining web thickness for a typical pentane run.[8] It can be shown that, for pentane tests, the outer web temperature changes very little until the last portion of the run after which it increases rapidly. In the last third of the run, the chamber pressure drops suddenly for the same test. This observation supports the possibility of sloughing caused by bulk heating of the propellant. The extent of this uncontrolled operation mode over the whole burn time is expected to be more significant for propellants with smaller absorptivities of radiation. In fact for a propellant to be practical its absorptivity must be increased over a minimum value by possibly adding materials that are good absorbers of radiation (that is, carbon black).

Even though the liquid layer combustion theory is developed for solid cryogenic propellants, it is applicable to any material that would form a liquid layer on their burning surfaces. In fact we have applied the theory on the homologous series of n-alkanes ($\rm C_nH_{2n+2}$). The results indicate that there exists an intermediate range of carbon numbers (16–50) corresponding to paraffin and Polyethylene (PE) waxes, where the material is both noncryogenic and generates high rates of entrainment of liquid droplets into the gas stream. The entrainment onset boundary and the relative entrainment rate for a paraffin wax with an average carbon number of 31 (melting temperature of approximately 67°C) are shown in Fig. 6 and Table 2, respectively. Surprisingly, the plot and table indicate that the predicted entrainment rate for the wax is comparable to that of the lower molecular weight pentane. This is because the average melt layer temperature of wax is much higher than the average melt temperature for pentane. The decrease in liquid viscosity and surface tension by increased temperature overcomes the increase caused by the molecular weight. Experiments conducted at Stanford University confirm the theory predictions.[8,20,21] The burning rate of a high grade paraffin wax (with a melting temperature of 69°C) as a function of mass flux is approximately four times faster than the burning rates of HTPB as indicated by Fig. 1. This makes the fast burning noncryogenic wax based propellants a perfect candidate for the future generation of hybrid rockets.

The liquid layer hybrid combustion theory also covers the classical propellants that form a liquid layer. The reason that the classical polymeric propellants such HDPE do not burn fast (even though they might form a liquid layer) is their highly viscous melt layers. For example, the melt layer viscosity of HDPE is predicted[8] to be

four orders of magnitude larger than the melt viscosity of pentane or wax. Naturally, at these super high viscosities, even at very high mass flux levels, the onset of entrainment is not achieved.

Conclusions

In this paper the hybrid diffusion limited theory is generalized to hybrid fuels that burn by forming a liquid layer. In the first step of our development, we determined the conditions required to form a melt layer with a thickness sufficient to produce entrainment. It is shown that the melt layer thickness can be a few hundred microns thick for typical cryogenic hybrid operating conditions. Next we have shown that these thin films with strong blowing could be unstable under hybrid operating conditions. Results reported in the literature are used to infer that the instabilities will result in the entrainment of droplets into the gas stream. The extra mass-transfer mechanism can potentially increase the regression rates an order of magnitude larger than the estimated rates from the classical theory. This is mainly because of the reduced effective heat of gasification, decreased blocking factor in the hybrid boundary layer and increased surface roughness.

The cryogenic hybrid rocket tests performed at the Air Force Research Laboratory and ORBITEC revealed regression rates 2–5 times larger than the expected rates estimated from the classical theory for low viscosity propellants such as pentane. The extended theory successfully predicted these very high regression rates observed in the cryogenic tests. The liquid layer theory also explained the slow burning rates of high viscosity propellants. Finally, the theory led to the conclusion that paraffin waxes will exhibit high regression rates comparable to pentane. Tests at Stanford on a laboratory-scale motor confirmed this prediction. The paraffin and PE waxes comprise a class of fast burning noncryogenic hybrid fuels with a wide spectrum of fuel properties. This provides the opportunity to satisfy a broad range of mission requirements for the next generation of hybrid rockets.

Acknowledgments

This work was partially supported by the NASA Ames Research Center, Moffet Field, California, and the Joint Institute for Aeronautics and Acoustics under Grants NCC2-55 and NCC2-1172. Additional, funds were provided by Stanford University.

References

[1]Marxman, G. A., Wooldridge, C. E., and Muzzy, R. J., "Fundamentals of Hybrid Boundary Combustion," *Progress in Astronautics and Aeronautics*, Vol. 15, 1964, p. 485–522.

[2]Larson, C. W., Pfeil, K. L., DeRose, M. E., and Carric, P. G., "High Pressure Combustion of Cryogenic Solid Fuels for Hybrid Rockets," AIAA Paper 96-2594, July 1996.

[3]Larson, C. W., DeRose, M. E., Pfeil, K. L., and Carric, P. G., "High Pressure Combustion of Cryogenic Hybrid Fuels in a Lab-Scale Burner," *Proceedings of the 1996 JANNAF Joint Propulsion Conference*, Chemical Propulsion Information Agency, John Hopkins Univ., CPIA, Columbia, MD, 1997, pp. 117–128.

[4]DeRose, M. E., Pfeil, K. L., Carric, P. G., and Larson, C. W., "Tube Burner Studies of Cryogenic Solid Combustion," AIAA Paper 97-3076, July 1997.

[5]Gramer, D., Rice, E., Knuth, W., and Clair, C. St., "Experimental Investigation of a Metallized Cryogenic Hybrid Rocket Engine," AIAA Paper 98-3509, July 1998.

[6]Clair, C. St., Rice, E., Knuth, W., and Gramer, D., "Advanced Cryogenic Solid Hybrid Rocket Engine Developments: Concept and Testing," AIAA Paper 98-3508, July 1998.

[7]Estley, P., Altman, D., and McFarlane, J., "An Evaluation of Scaling Effects for Hybrid Rocket Motors," AIAA Paper 91-2517, June 1991.

[8]Karabeyoglu, M. A., "Transient Combustion in Hybrid Rockets," Ph.D. Dissertation, Department of Aeronautics and Astronautics, Stanford Univ., CA, Aug. 1998.

[9]Altman, D., and Humble, R., "Hybrid Rocket Propulsion Systems," *Space Propulsion Analysis and Design*, edited by R. W. Humble, G. N. Henry, and W. J. Larson, McGraw–Hill, New York, 1995, p. 365–441.

[10]Karabeyoglu, M. A., and Cantwell, B. J., "Combustion of Liquefying Hybrids—Part II: Stability of Liquid Films," *Journal of Propulsion and Power* (submitted for publication).

[11]Lang, L., *Absorption Spectra in the Infrared Region*, Butterworths, London, 1974, pp. 10–15.

[12]Bentley, F. F., Smithson, L. D., and Rozek, A. L., *Infrared Spectra and Characteristic Frequencies ~700-300 cm^{-1}*, Interscience, New York, 1968, pp. 21–23.

[13]Seigel, R., and Homel, J. R., *Thermal Radiation Heat Transfer*, Hemisphere, Washington, DC., 1992, pp. 412–538.

[14]Dauber, T. E., and Danner, R. T., *Physical and Thermodynamic Properties of Pure Chemicals, Data Compilation*, Taylor and Francis, Washington, DC, 1997.

[15]Gater, R. A., and L'Ecuyer, M. R. L., "A Fundamental Investigation of the Phenomena that Characterize Liquid Film Cooling," *International Journal of Heat and Mass Transfer*, Vol. 13, No. 3, 1970, pp. 1925–1939.

[16]Nigmatulin, R., Nigmatulin, B., Khodzaev, Y. A., and Kroshilin, V., "Entrainment and Deposition Rates in a Dispersed-Film Flow," *International Journal of Multiphase Flow*, Vol. 22, No. 1, 1996, pp. 19–30.

[17]Ishii, M., and Grolmes, M. A., "Inception Criteria for Droplet Entrainment in Two Phase Concurrent Film Flow," *AIChE Journal*, Vol. 21, No. 2, 1975, pp. 308–318.

[18]Nigmatulin, B. I., Klebanov, L. A., and Kroshilin, A. E., "Critical Heat Transfer in the Transient Boiling of Vapour-Liquid Annular-Mist Flows," *High Temperature*, No. 18, No. 6, 1980, pp. 927–935.

[19]Marxman, G. A., "Combustion in the Turbulent Boundary Layer on a Vaporizing Surface," *Tenth Symposium on Combustion*, 1965, pp. 1337–1349.

[20]Karabeyoglu, M. A., Cantwell, B. J., and Altman, D., "Development and Testing of Paraffin-Based Hybrid Rocket Fuels," AIAA Paper 2001-4503, July 2001.

[21]Karabeyoglu, M. A., Altman, D., and Cantwell, B. J., "High Regression Rate Hybrid Rocket Fuels," Patent pending.